Identification of stratospheric disturbance information in China based on round-trip intelligent sounding system

Yang He[1], Xiaoqian Zhu[1], Zheng Sheng*[1], Mingyuan He[1]

[1] College of Meteorology and Oceanography, National University of Defense Technology, Changsha, 410073, China

Correspondence to: Zheng Sheng (19994035@sina.com)

Abstract. Assessing the role of physical processes in the stratosphere under climate change has been one of the hottest topics over the past few decades. However, due to the limitation of detection technique, the stratospheric disturbance information from in situ observation is still relatively scarce. The round-trip intelligent sounding system (RTISS) is a new detection technology developed in recent years, which can capture atmospheric fine structure information of the troposphere and stratosphere through the three-stage (rising, flat-floating, and falling) detection. Based on the structure function and singular measure, we quantify the stratospheric small-scale gravity wave (SGW) over China by Hurst parameter and intermittency parameter, and discuss its relationship with inertia-gravity wave (IGW). The results show that the enhancement of the SGWs in the stratosphere is accompanied by the weakening of the IGWs below, which is closely related to the Kelvin-Helmholtz instability (KHI), and is conducive to the transport of ozone to higher altitudes from lower stratosphere. The parameter space (H1, C1) shows sufficient potential in the analysis of stratospheric disturbances and their role in material transport and energy transfer.

1 Introduction

Gravity waves (GWs) are waves generated by gravity and are widespread in the earth's atmosphere. GWs are excited by wave sources in the troposphere, including topography, convection and wind shear, etc, and propagate from the troposphere to the stratosphere and higher altitudes (Alexander et al., 2010; Fritts and Alexander, 2003, 2012). During upward propagation of GW, due to the decrease of atmospheric density and the increase of wave amplitude, the influence of GW on the surrounding atmosphere is increasingly important. This effect is mainly caused by the unstable of GWs with increasing amplitude, or the breaking of GWs when they encounter the "critical layer", thus changing the circulation and structure of the atmosphere by dissipating energy and momentum (Allen and Vincent, 1995; Hertzog et al., 2012).

In order to improve the simulation of the main average characteristics of the atmosphere by numerical weather prediction (NWP) and general circulation model (GCM), it is necessary to describe important physical processes in the atmosphere more accurately and efficiently (Kim et al., 2003). The scale of GW is relatively small and cannot be resolved in models with relatively rough resolution, so it is necessary to use a parameterization to describe the influence and interaction of GW on

30   larger-scale dynamic process. GW parameterization is now a key component of almost all large-scale atmospheric models. However, due to the lack of observational constraints and insufficient understanding of the mechanism, it also restricts the prediction accuracy and simulation ability of the models (Plougonven et al., 2020).

Assessing the role of stratospheric physical processes under climate change is one of the hottest topics in the past few decades (SPARC, 2022; Tian et al., 2023). Gravity wave, as one of the important physical processes in the stratosphere, has
35   been extensively studied, based on radiosonde (Kinoshita et al., 2019; Moffat-Griffin et al., 2013), rocket (Eckermann et al., 1995), radar (Alexander et al., 2017; Huang et al., 2017), remote sensing (Wright et al., 2016; Guo et al., 2021) and other detection methods. Limited by the detection technology, relatively little research has been carried out on the fine structure of the stratospheric atmosphere. Aircraft observation can only be used for specific design tasks (Zhang et al., 2015), with little continuous data accumulation. Super-pressure balloons can provide stratospheric GW field information on particular zonal
40   circles with long-duration observation (Alexander et al., 2021; Hertzog et al., 2008), though it is not currently applicable to local areas within countries.

At present, the stratospheric disturbance information in the horizontal direction is still relatively scarce in China, and the introduction of the flat-floating information can help to improve the forecasting effect of the model and deepen the understanding of stratospheric dynamic processes (Laroche et al., 2013; Stephen A et al., 2015). The round-trip intelligent
45   sounding system (RTISS) is a new detection technology developed in recent years (Cao et al., 2019), which can capture atmospheric fine structure information of the troposphere and stratosphere through the three-stage (rising, flat-floating, and falling) detection. For the first time, this paper shows a relatively complete analysis of atmospheric disturbance information in the horizontal direction of the stratosphere in China through RTISS, and provides an innovative result for the evaluation of physical processes in the stratosphere.

2 Observation from RTISS

2.1 Introduction to experimental data

The data used in this paper is from experimental project of round-trip intelligent sounding system (RTISS), covering six sites including Yichang, Wuhan, Anqing, Changsha, Nanchang, and Ganzhou in China. RTISS can realize the three-stage detection including "rising, flat-floating, and falling", which has become an important source for the analysis of atmospheric
55   disturbance information in the horizontal direction of the stratosphere (Cao et al., 2019; He et al., 2022a). The release time span is from June 1 to July 10 (summer), and from October 13 to November 18 (autumn) in 2018.

The details of the observation experiment are shown in Figure 1. The flat-floating height covers the range of 18–32 km, mainly concentrated in 26–30 km (Figure 1a), and the variation of height over time during the entire detection process is shown in Fig. A1. Six sites are all located in southeast China (Figure 1b). The balloon trajectories can directly reflect the stratospheric
60   wind field characteristics over the corresponding sites (Figure 1 c–h). In summer, the stratosphere is mainly dominated by

2

easterly winds, with relatively stable circulation (more consistent trajectories), while in autumn, circulation changes more

frequently (more divergent trajectories).
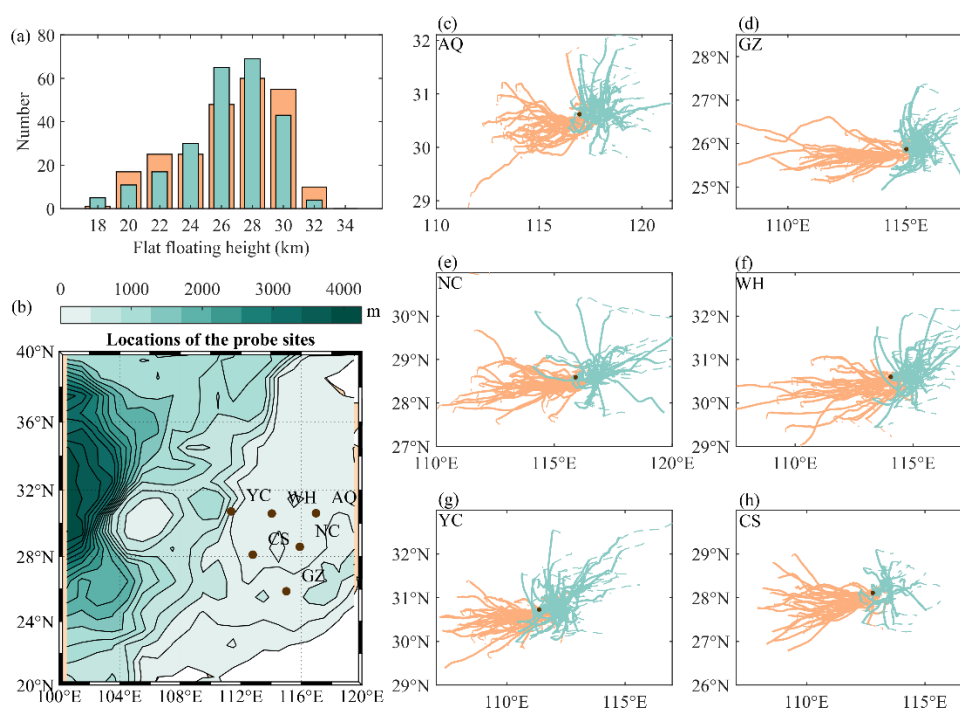
Figure 1. (a) Histogram of flat-floating height, (b) A topographic map of the RTISS release sites and nearby areas, and the trajectories of RTISS over (c) Anqing, (d) Ganzhou, (e) Nanchang, (f) Wuhan, (g) Yichang, and (h) Changsha. The black dots represent the release sites, the dashed lines represent trajectories during rising and falling stages, and the solid lines represent trajectories during flat-floating stage. In order to better compare the results of different sites, the axis of the c–h subgraph is unified into the same geographic width (10°×4°).

2.2 Detection principle and quality control

RTISS aims to maintain a relatively low cost while achieving encrypted observations (rising and falling) several hours

apart in the vertical direction, as well as continuous high-frequency observations (1s) for several hours at a specific altitude

(flat-floating), to capture the atmospheric fine structure information from the troposphere to the stratosphere, including wind

field, temperature, air pressure and relative humidity. The sounding instrument carries the Beidou navigation system and

meteorological sensor. The Beidou navigation system provides positioning information (longitude, latitude, altitude) that can

be used to calculate the horizontal wind field. The uncertainty of wind speed is 2 m/s during rising stage and 4 m/s during flat-

floating stage. The sensor module can be used to obtain temperature, relative humidity, and air pressure, which consists of

three parts: (1) a negative temperature coefficient (NTC) thermistor sensor for temperature measurement, with an uncertainty

of 0.8 K during rising stage and 2.8 K during flat-floating stage; (2) a piezoresistive sensor for air pressure measurement, with

80 an uncertainty of 1 hPa during the rising stage and flat-floating stage; and (3) a humidity-sensitive capacitance sensor, with an uncertainty of 10% RH during the rising stage, while it is ignored during flat-floating stage with poor data quality. The uncontrolled, high-velocity descent through parachute during falling stage may influence measurement quality with a strong pendulum motion (Jorge et al., 2021), so we do not consider the data in this stage.

The detection principle is simply summarized as follows: in the rising stage, the two-ball method (an inner balloon inside

85 an outer balloon) is used to carry the radiosonde up and make real-time measurements. When a predetermined height is reached, the outer ball is exploded, at that time, the buoyancy of the inner ball is just equal to the gravity of the carrying instrument, and it drifts with the wind at the predetermined height with a quasi-horizontal movement. When the balloon floats for several hours to reach the predetermined area, the radiosonde and the inner ball are separated by a fuse device, then the parachute above the instrument opens, carrying the instrument descends.

90 It is known that balloon payload can have a pendulum motion (Andreas et al., 2016), and we have selected the appropriate smooth fitting interval to eliminate its effect. An integer multiple of the swing period is used as the smooth fitting interval, and the symmetry of the swing is used to compensate for the swing deviation. Using the average smoothed position coordinates, the first derivative is obtained by linear fitting to obtain the speed, and the second derivative is obtained by quartic fitting to obtain the acceleration. Then wind speed and wind direction can be obtained after that.

95 In order to ensure the premise of approximate constant height, we need to sift through all the flat-floating data, and only data sets with a long enough flat-floating time (longer than 3–4 hours) and relatively good flat-floating quality (the difference between the maximum and minimum height is within several hundred meters) are selected. Along the separation distance direction, the flat-floating distance is usually tens of kilometers to hundreds of kilometers, and the fluctuation of several hundred meters in the vertical direction can still be approximated as quasi-horizontal movement. The original data is tested for

100 horizontal consistency, and then re-interpolated to a uniform interval after the outlying and missing values are removed.

3 Analysis method

3.1 Third-order structure function

In order to effectively identify the atmospheric disturbance information obtained by RTISS, we consider combining the results from the rising and flat-floating stages for analysis, while the falling stage is not included due to the relatively poor data

105 quality. We assume that RTISS can capture the same weather system during the rising and flat-floating stages due to the continuous observation in space and time. The observation results in the horizontal and vertical directions can just complement each other, which is currently impossible for other single observations.

We use the third-order structure function $S_3(r)$ to identify GWs and turbulence (Text S2). This method was earlier used in aircraft observation data (Cho and Lindborg, 2001). At the tail of the third-order structure function (turbulence subrange),

110 the r slope represents the occurrence of turbulence, while in the larger scales (GW subrange), the r^2 and r^3 slope represent the

unstable and stable GW, respectively (Lu and Koch, 2008; He et al., 2022a). The calculation is as follows (Cho and Lindborg, 2001; Lindborg, 1999):

$$S_3(r) = \langle [\delta u_L(r)]^3 \rangle + 2\langle \delta u_L(r)[\delta u_T(r)]^2 \rangle = -\frac{4}{3}\varepsilon r, \tag{1}$$

Among them, $\langle . \rangle$ is the ensemble average, r is the separation distance, and ε is the energy dissipation rate. L and T
115 represent the directions parallel to and perpendicular to the separation distance, respectively. The balloon trajectory during flat-floating stage is not a straight line, so we decompose it into the zonal and meridional directions, and take the direction of the longer projection distance as the separation distance direction. The raw data is uniformly interpolated to the average step along the separation distance direction. Separation distance $r = l \times 2^n$, $n = 0,1 \dots, N$. l is the average step along the separation distance direction, and N is limited by the maximum data length. δu_L (δu_T) is a data set that contains the difference in
120 velocities with a separation distance r on all grid points along separation direction (perpendicular to the separation direction). A positive value of $S_3(r)$ represents upscale energy cascades (from small to large scales), while a negative value of $S_3(r)$ represents downscale energy cascades (from large to small scales) (Lindborg, 1999).

3.2 Hurst index and intermittent parameter

Similar to Eq. (1), the multi-order structure function is defined as：
125
$$S_q(r) = \langle |u_L(x+r) - u_L(x)|^q \rangle = \langle |\delta u_L(r)|^q \rangle, \tag{2}$$

Because u_L is the quasi-Lagrangian measurement result in the horizontal direction, $\delta u_L(r)$ can be regarded as a position-independent statistical results. Assuming that this process is scale-invariant and self-similar, $S_q(r)$ can be scaled to (Lu and Koch, 2008):

$$S_q(r) = C_q r^{\zeta(q)}, q \geq 0, \tag{3}$$

130 Where C_q is a constant and $\zeta(q)$ is a function of order q. From this we can define a monotone, non-increasing function (Marshak et al., 1997):

$$H(q) = \frac{\zeta(q)}{q}, \tag{4}$$

Here we choose H1=$H(1)$ as the Hurst index, with a value between 0-1. The larger the H1, the smoother the data sequence and the fewer wave packets superimposed on it, and vice versa.
135 Statistical analysis called singularity measurement can be used to reflect the intermittency of the data sequence (Marshak et al., 1997), a non-negative normalized η-scale gradient field is defined by a second-order structure function (Lu and Koch, 2008):

$$\varepsilon(\eta; x) = \frac{|\delta u_L(x,\eta)|^2}{\langle |\delta u_L(x,\eta)|^2 \rangle}, \eta \leq x \leq L - r, \tag{5}$$

Where L is the maximum length of the data, and $\eta = 4l$ is four times the Nyquist wavelength. The measurements at
140 different separation distances r can be expressed by the results of spatial averaging：

$$\varepsilon(r;x) = \frac{1}{r}\int_x^{x+r}\varepsilon(\eta;x')\,dx', \ \eta \leq x \leq L-r, \tag{6}$$

The self-similarity of fluctuations makes the q-order measurement expressed as:

$$\langle\varepsilon(r;x)^q\rangle = \langle\varepsilon(r)^q\rangle \propto r^{-K(q)}, q \geq 0, \tag{7}$$

By linearly fitting the $\varepsilon(r)$ curves of different orders q, the $K(q)$ curve can be obtained. Then the generalized dimension
145   is introduced：

$$D(q) = 1 - \frac{K(q)}{q-1} \tag{8}$$

The intermittent nature of fluctuations can be expressed as：

$$C_1 = 1 - D(1) = 1 - \lim_{q\to1}D(q) = \lim_{q\to1}\frac{K(q)}{q-1} = K'(1), \tag{9}$$

C1 is an intermittent parameter with a value between 0-1, reflecting the singularity of the fluctuation. The larger the value,
150   the more intermittency in nonstationary data, and the more singular the fluctuations. According to Eq. (5) and Eq. (7), it can
be seen that the premise of Eq. (9) here is that K(1)=0 (Lu, 2008).

## 4 Results and Discussion

4.1 Determination of scale interval

When no turbulence occurs (there is no r slope at the tail of the third-order structure function), the calculated H1 and C1
155   both comes from the fitting interval of the GW subrange. When turbulence occurs (there is an r slope at the tail of the third-
order structural function), the fitting interval of turbulence and GW should be distinguished, and the slope at the corresponding
scale should be calculated separately. Taking into account the different separation distances of different data, the scale range
corresponding to the calculated parameters will vary. However, in order to facilitate comparison, we use the separation distance
r closest to 500 m (< 500 m) as the turbulent outer scale R_t, and the separation distance closest to 5 km (< 5 km) as the gravity
160   wave outer scale R_w, aiming to identify small-scale, high-frequency GW with a spatial scale of several kilometers. The fitting
intervals of turbulence and gravity waves are [η, R_t] and [R_t, R_w], respectively.

During statistical analysis, in order to compare the GWs that did not accompany the turbulence with the GWs that
accompanied the turbulence, the calculated H1 and C1 are unified into the same fitting interval [η, R_w]. When turbulence
occurs in the tail, the C1 value obtained from [η, R_w] interval will also be larger, which means that C1 calculated over a wider
165   range can also recognize the occurrence of turbulence. In order to obtain C1 in [η, R_w] fitting interval from (9), it is necessary
to ensure that K(1)=0 (or approximately close to 0), thereby discarded some unsatisfactory cases.

The velocity increments $\delta u_L(r)$ is the key process for calculating the disturbance parameters from flat-floating data, and
has shown good robustness within the separation distance of small-scale gravity waves and turbulence (He et al., 2022a).
therefore, the results will not be affected by the fluctuation of flat-floating height, as well as the swing of the balloon.

4.2 Quantification of atmospheric disturbance information

170

Taking the data from the Yichang site as an example, to illustrate how to identify the disturbance information from the flat-floating data. The multi-order structure function $S_q(r)$ is shown in Figure 2a. Using the $S_q(r)$ curve of q=1 for linear fitting, H1 can be obtained, with a value of 0.68. From third-order structure function, a downscale energy cascade (from large to small scales) can be seen from the third-order structure function, with a r^3 slope indicating that no turbulence has been

175   observed within the resolved resolution. Figure 2c is the relationship between the q-order singularity measure $\langle \varepsilon(r; x)^q \rangle$ and the separation distance r in log-log coordinate, through which C1 is calculated with a value of 0.08 (Figure 2d). Using the criterion proposed in section 2 for the identification of GW state, this case can be identified as a stable GW, and the GW scale quantified by (H1, C1) is 5.1 km.
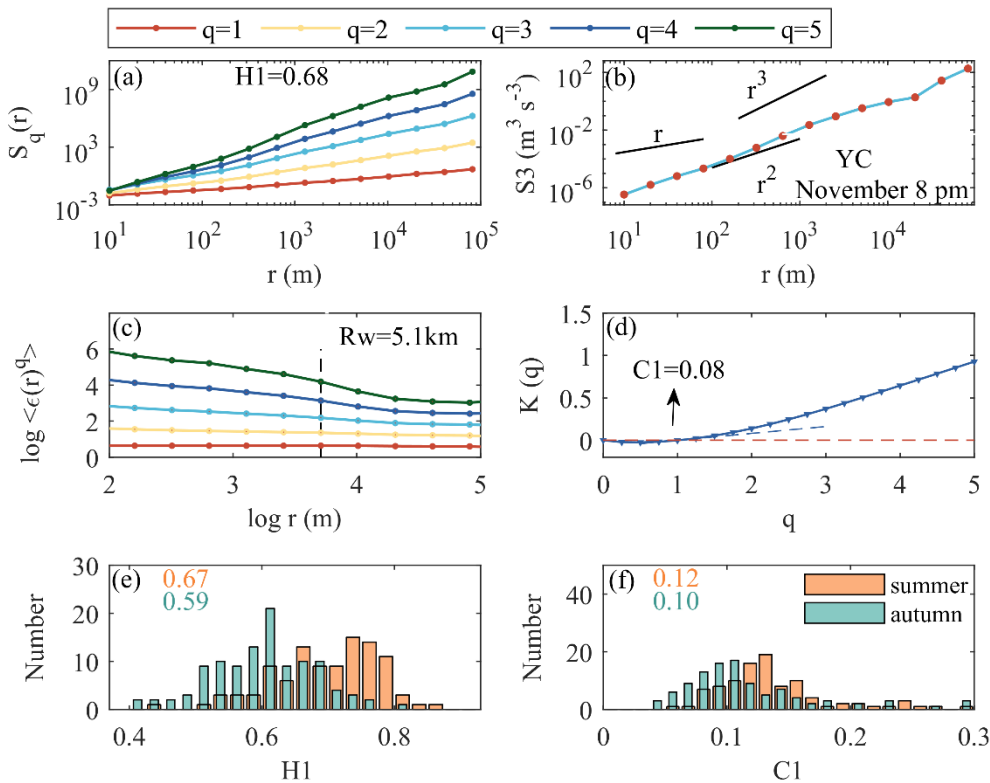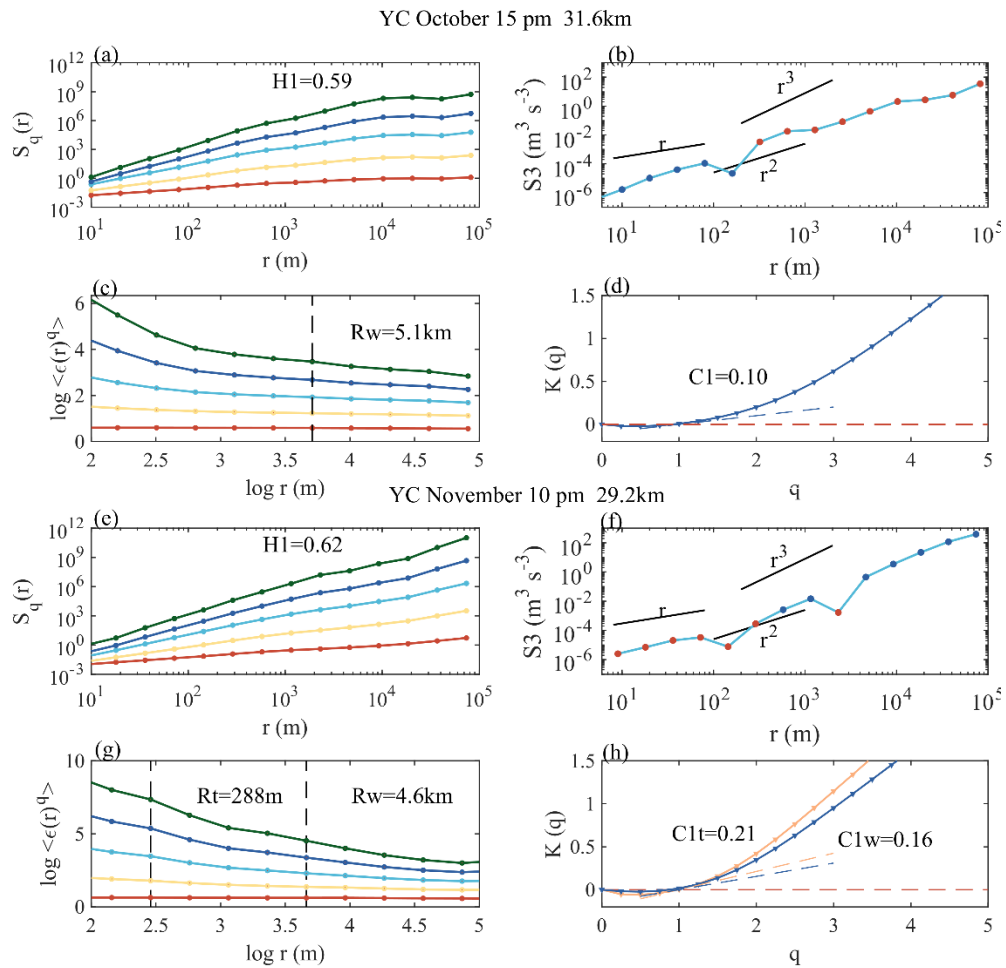

180 **Figure 2. (a) Multi-order structure function, (b) third-order structure function (the red dots represent negative values), (c) multi-order singular measure, (d) slope K(q) obtained from Yichang site on November 8. Histogram of (e) Hurst index and (f) intermittent parameter from all flat-floating data over the six sites.**

Figure 3 shows cases for unstable GW and the coexistence of GW and turbulence. The case for Yichang data at October

185   15 pm can be identified as an unstable GW, and the GW is quantified as (0.59, 0.10), with a scale of 5.1 km. The case for

Yichang data at November 10 pm can be identified as a GW coexist with turbulence, and the GW is quantified as (0.62, 0.16), with a scale of 4.6 km. Meanwhile, the intermittency parameter for the recognized turbulence is 0.21 with a scale of 288 m.

Therefore, when the stratospheric disturbance information is relatively abstract, the disturbance intensity can be quantified using (H1, C1) as a reference for mutual comparison. Figure 2e and 2f show the histogram of Hurst parameters and intermittent parameters of all data from the six sites, respectively. In summer, the H1 (C1) value is mainly concentrated in the range of 0.6–0.8 (0.10–0.22), while in autumn, the H1 (C1) value is mainly concentrated in the range of 0.5–0.7 (0.08–0.20). Compared with summer, stratospheric wave disturbances in autumn have a lower H1 and C1 distribution.


Figure 3. (a) Multi-order structure function, (b) third-order structure function, (c) multi-order singular measure and (d) slope K(q) obtained from Yichang site at October 15 pm, and (e) multi-order structure function, (f) third-order structure function, (g) multi-order singular measure and (h) slope K(q) obtained from Yichang site at November 10 pm.

8

## 4.3 Statistical results of disturbance parameters

Based on the data during the rising stage, we use hodograph analysis to extract IGW parameters (Bai et al., 2016; Huang

200   et al., 2018), with a height interval of 18–25km, thereby obtaining parameters including vertical wavelength, horizontal wavelength, intrinsic frequency, propagation direction (anticlockwise from y axis), kinetic energy, potential energy, and momentum flux. In order to eliminate the error caused by the random movement of the balloon, the data is uniformly interpolated to an interval of 50 m. The total energy is the sum of kinetic energy and potential energy. Based on Thorpe analysis (Ko & Chun, 2022; Thorpe, 1977; Wilson et al., 2011), the atmospheric turbulent layer is identified from the sorted potential

205   temperature profile, thereby obtaining parameters including Thorpe length, turbulent layer thickness, turbulent kinetic energy dissipation rate, and turbulent diffusion coefficient. Optimal smoothing and statistical tests are used to distinguish "overturn" caused by real turbulent motion and artificial "inversion" caused by instrument noise and balloon motion (Wilson et al., 2011).

The distribution of inertial gravity wave and turbulence parameters is shown in Figure 4. The wavelength, intrinsic frequency, and energy of IGWs in summer and autumn show no obvious differences. The momentum flux in summer has a

210   significant positive shift, the net zonal momentum flux is eastward with easterly winds dominated in the stratosphere. The dominant propagation directions of IGWs in summer and autumn are northeast and southwest respectively, due to the effect of "critical layer filtering" (Eckermann, 1995). For disturbances from small-scale turbulence, there is no obvious difference between the Thorpe length and turbulence thickness in summer and autumn. In autumn, the turbulent kinetic energy dissipation rate and turbulent diffusion coefficient have a more ideal Gaussian distribution with smaller peak value, indicating that the

215   wave source is more single and the turbulence activity is weaker than that in summer. The deviation of turbulence peaks in different studies may come from the intermittency of turbulence, sensor performance, and regional source characteristics (Ko and Chun, 2022; Zhang et al., 2019; Lv et al., 2021).
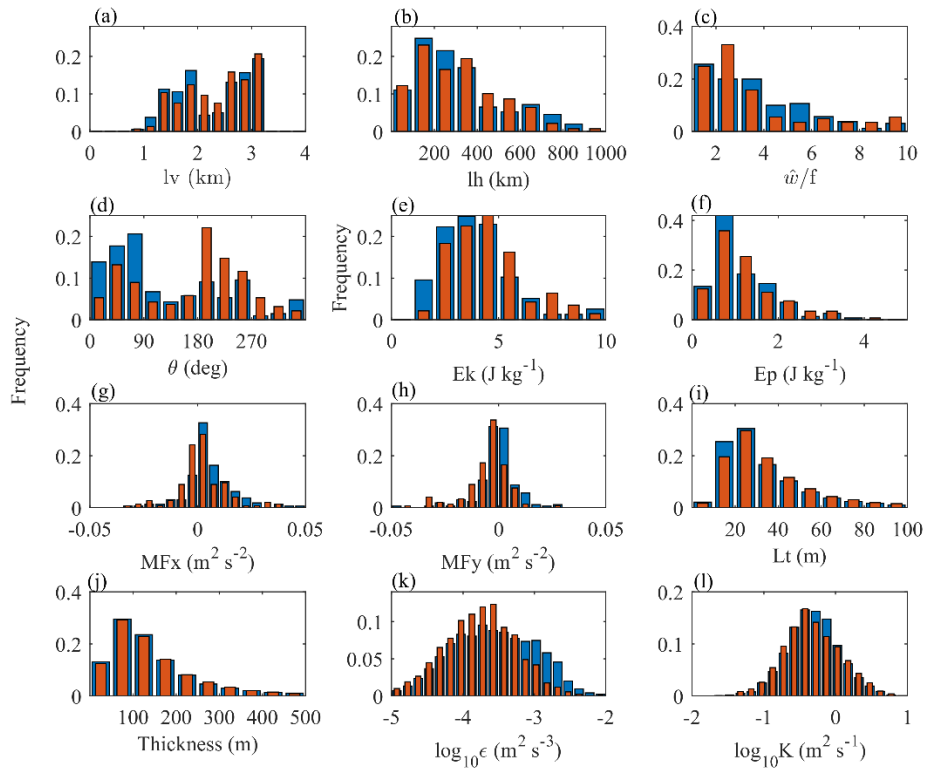
Figure 4. Histogram of disturbance parameters for IGW including (a) vertical wavelength, (b) horizontal wavelength, (c) intrinsic frequency, (d) horizontal propagation direction, (e) kinetic energy, (f) potential energy, (g) zonal momentum flux, and (h) meridional momentum flux. Histogram of disturbance parameters for turbulence including (i) Thorpe length, (j) Turbulent layer thickness, (k) Turbulent kinetic energy dissipation rate, and (l) turbulent diffusion coefficient.

The results of H1 and C1 over the six sites are shown in Figure 5. Compared with the coexistence of GW and turbulence or unstable GW, stable GW tends to have a larger H1 and a smaller C1. Compared with other sites, there is always a relatively stronger fluctuation singularity (greater C1) for stratospheric SGW over Ganzhou, no matter in summer or autumn, which may be related to its unique geographical location (surrounded by mountains with lower latitude). The cases in red rectangles are the detection of adjacent times when the flat-floating height is close, which is convenient to compare the third-order structure functions and the wind speed disturbance behind the different (H1, C1), the result is shown in Figure 6. It can be intuitively seen from the results of the wind speed disturbance that, the lower the H1 value, the rougher the data sequence, accompanied by more wave packets; the larger the C1, the more singular the fluctuation, accompanied by stronger disturbances deviating from the average state. This is the first time that a relatively comprehensive (multi-site, multi-time) result of stratospheric atmospheric disturbance information in the horizontal direction has been given by balloon observation in China, which can provide an intuitive reference for the cognition of the stratospheric atmospheric environment.

10
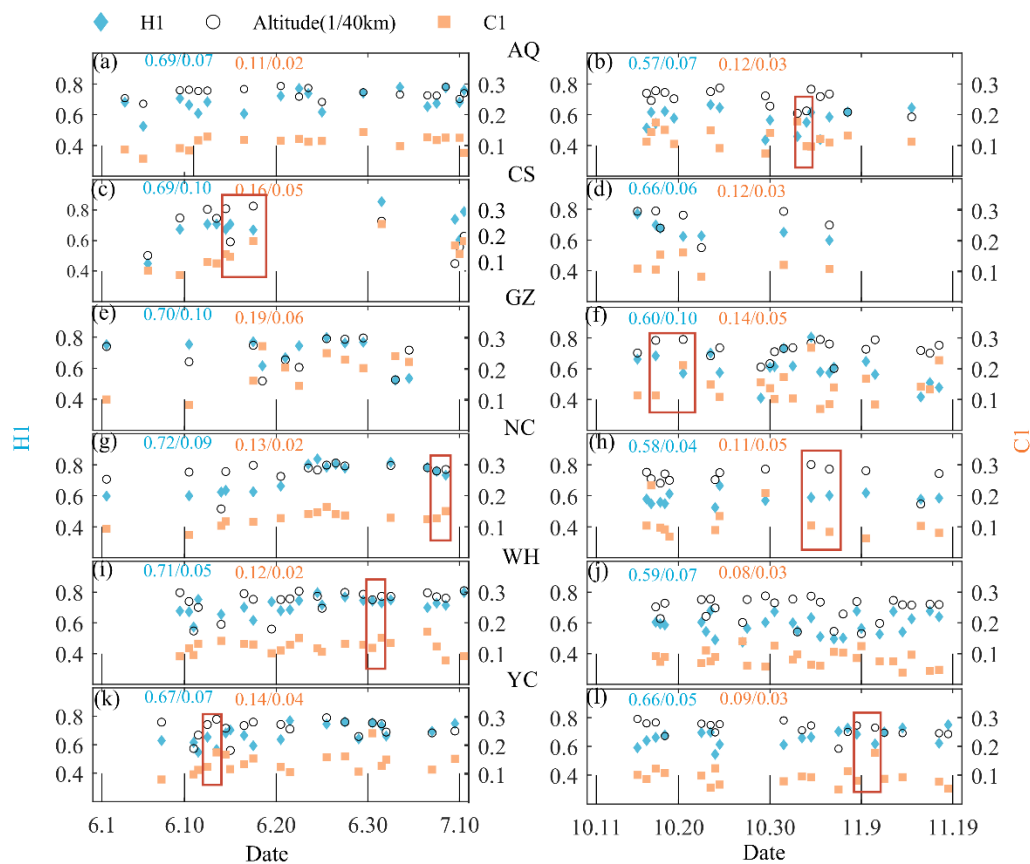
Figure 5. The atmospheric disturbance parameters (H1, C1) and the corresponding average flat-floating height (scaled to 1/40) obtained over the six sites in summer (left panel) and autumn (right panel), the mean and standard deviation of H1 and C1 are marked in blue and yellow, respectively.
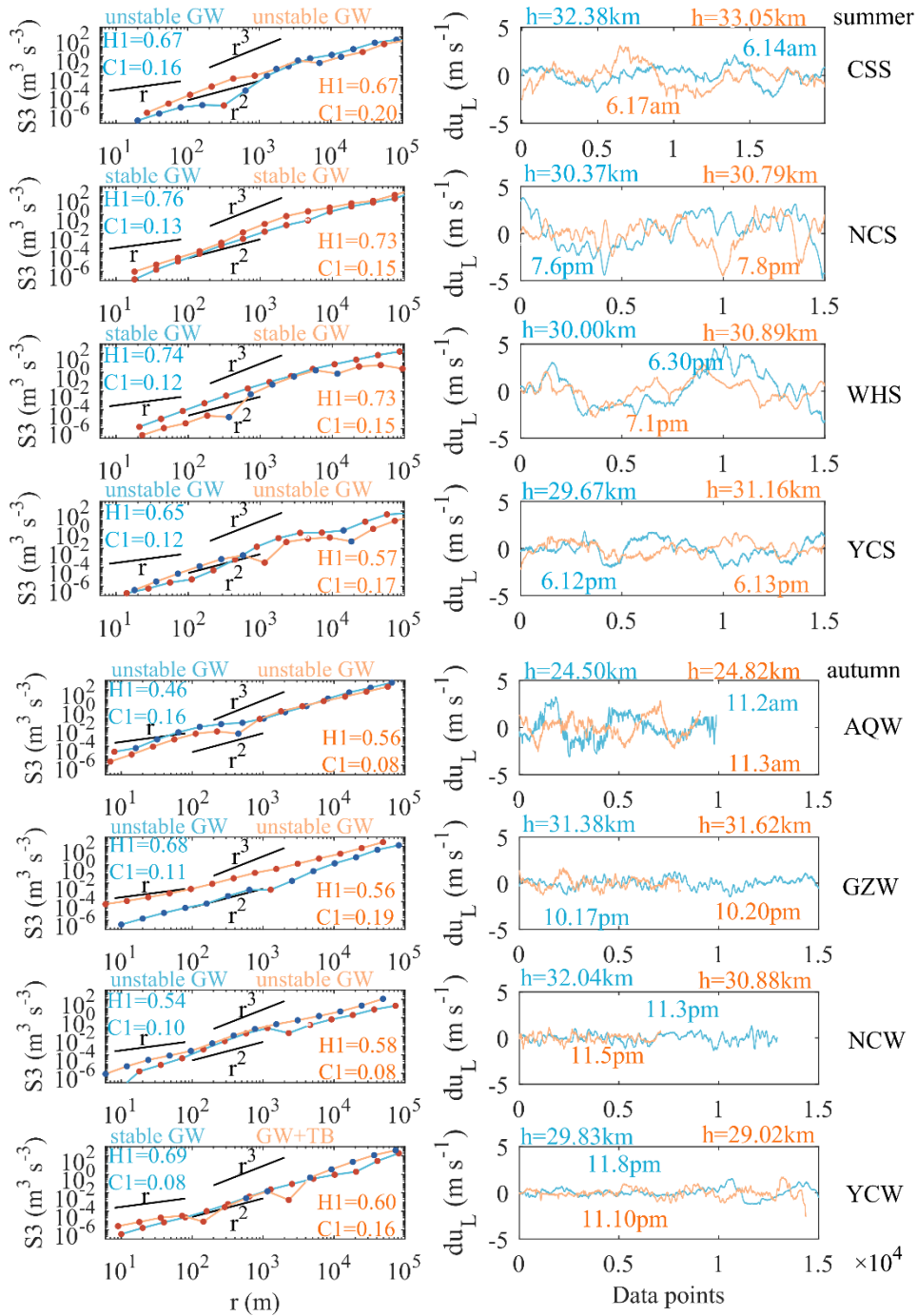
Figure 6. The atmospheric disturbance parameters (H1, C1) and the corresponding average flat-floating height (scaled to 1/40) obtained over the six sites in summer (left panel) and autumn (right panel), the mean and standard deviation of H1 and C1 are marked in blue and yellow, respectively.

4.4 Potential links between multiscale fluctuations

Although there are different methods for quantifying wave disturbances, linking detection results from different profiles (for example, in the vertical and horizontal directions) is still a challenge and an observation gap. Taking the detection results from RTISS as an opportunity, the possible connection between wave disturbances obtained by different quantitative methods is discussed, and the result is shown in Figure 7. It should be noted here that the wave disturbance extracted from the flat-floating data is a small-scale, high-frequency GW with a spatial scale of several kilometers, while the wave disturbance extracted from the rising data is an IGW with a spatial range of several hundred kilometers. There is no clear linear correlation between H1 and C1 (Figure 7a). C1 can reflect the intensity of turbulence mixing and is highly intermittent and random, which is not related to height (Figure 7b). In contrast, there is a significant positive linear correlation between H1 and height (Figure 7c). As height increases, the entire data series tends to be smoother.\
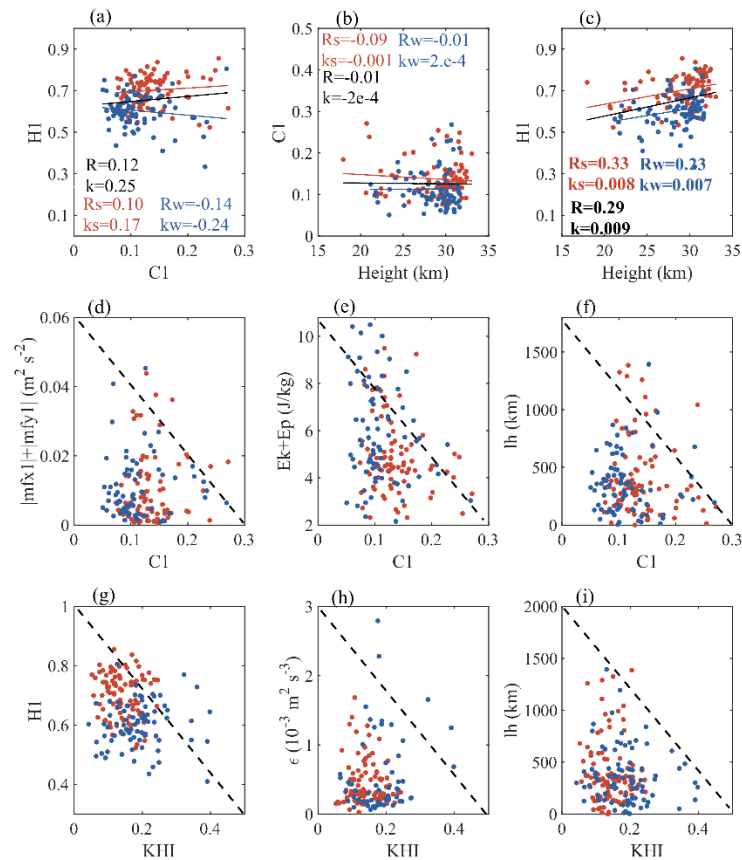
Figure 7. Scatter plots of (a) H1 versus C1, (b) C1 versus height, (c) H1 versus height, (d) momentum flux versus C1, (e) total energy versus C1, (f) horizontal wavelength versus C1, (g) H1 versus KHI (ratio of 0 < Ri < 0.25), (h) ε versus KHI, and (i) horizontal wavelength versus KHI. Blue and red dots represent summer and autumn. The blue, red and black lines in (a)–(c) represent linear fitting results of summer, autumn and all data, respectively.

Due to the limitations of the sample size and the different detection objects, the linear correlation between these variables may not be statistically significant, so we pay more attention to the change trend between them. With the increase of C1, the momentum flux, total energy, and horizontal wavelength of IGW are more concentrated in a lower range (Figure 7d–f). Considering that the wave disturbance in the stratosphere is likely to be related to KHI (He et al., 2020b; Lu and Koch, 2008), here the ratio of $0 < Ri < 0.25$ between 15–25 km is used to represent the Kelvin- Helmholtz instability (KHI) to explore its connection with atmospheric disturbances. As KHI increases, the horizontal wavelength of IGW decreases (Figure 7i), while the data sequence of SGW tends to be rougher (Figure 7g). The turbulent kinetic energy dissipation rate (ε) increases first and then decreases with the increase of KHI (Figure 7h). This is because the increase of KHI is conducive to the generation of turbulence, however, when the KHI reaches a certain threshold value, the turbulent layer cannot be maintained and begins to decay, resulting in a weakening of turbulence activity (He et al., 2020a).

From the above results, it can be seen that the increased instability of SGWs in the stratosphere will be accompanied by the weakening of IGWs below. The KHI that appears in an unstable shear due in part to IGW (Abdilghanie and Diamessis, 2013) is likely to be the excitation source of small-scale, high-frequency GW propagating to higher altitudes. This phenomenon has also been confirmed in numerical simulation in the mesosphere and higher altitudes (Dong et al., 2023).

**4.5 Relation between parameter space and ozone transport**

The transport of Ozone and its changing trends is one of the important issues concerned in stratospheric research, which is closely related to the atmospheric radiation balance and global warming (Tian et al., 2023; Fei Xie et al., 2016; Jiankai Zhang et al., 2022). The ozone and potential vorticity (PV) have good consistency, which can be regard as good indicators for studying the stratospheric material transport process (Allaart et al., 1993; Newell et al., 1997). Considering that the GW process plays an important role in the transport of ozone between the upper and lower layers (Gabriel, 2022), we hope to explore whether there is a direct connection between the quantitative indicator of wave disturbance and ozone.

Based on the ERA5 reanalysis data, the ozone mass mixing ratio (OMR) and PV at different pressure layers that matched the detection are selected. The release time of flat-floating detection is divided into two periods, morning and evening. The release time is basically 23UTC (7:00 Beijing time) and 11UTC (19:00 Beijing time). Taking into account the rise time of nearly 1 hour, the data of the flat-floating period exactly corresponds to 00UTC and 12UTC of ERA5. Then according to the latitude and longitude range covered by RTISS during flat-floating stage, the OMR and PV obtained from the ERA reanalysis data are averaged in the corresponding area. The matching results of different air pressure layers (200hPa, 175hPa, 150hPa, 125hPa, 100hPa, 70hPa, 50hPa, 30hPa, 20hPa, 10hPa, 5hPa, 3hPa, 2hPa, 1hPa) are calculated.

Figure 8 shows the possible connection between C1 and these two indicators (OMR and PV). The pressure layers selected here correspond to the height above and below the flat-floating interval, in order to distinguish them from the height range where small-scale GWs are detected. In the lower stratosphere, there is a significant positive correlation between ozone and PV, while in the middle stratosphere, there is a significant negative correlation between the two. For SGWs detected during flat-floating stage, the larger the C1, the weaker the PV in the stratosphere, accompanied by the reduction of IGWs (Kalashnik

and Chkhetiani, 2017). This is consistent with the result that the higher C1 corresponds to the lower IGW energy below in

295   Figure 7. The more intermittency of SGWs, the less (more) ozone below (above), thereby forming an enhanced ozone transport between them. The significant positive (negative) correlation between C1 and ozone concentration above (below) further support this argument (Figure 9).
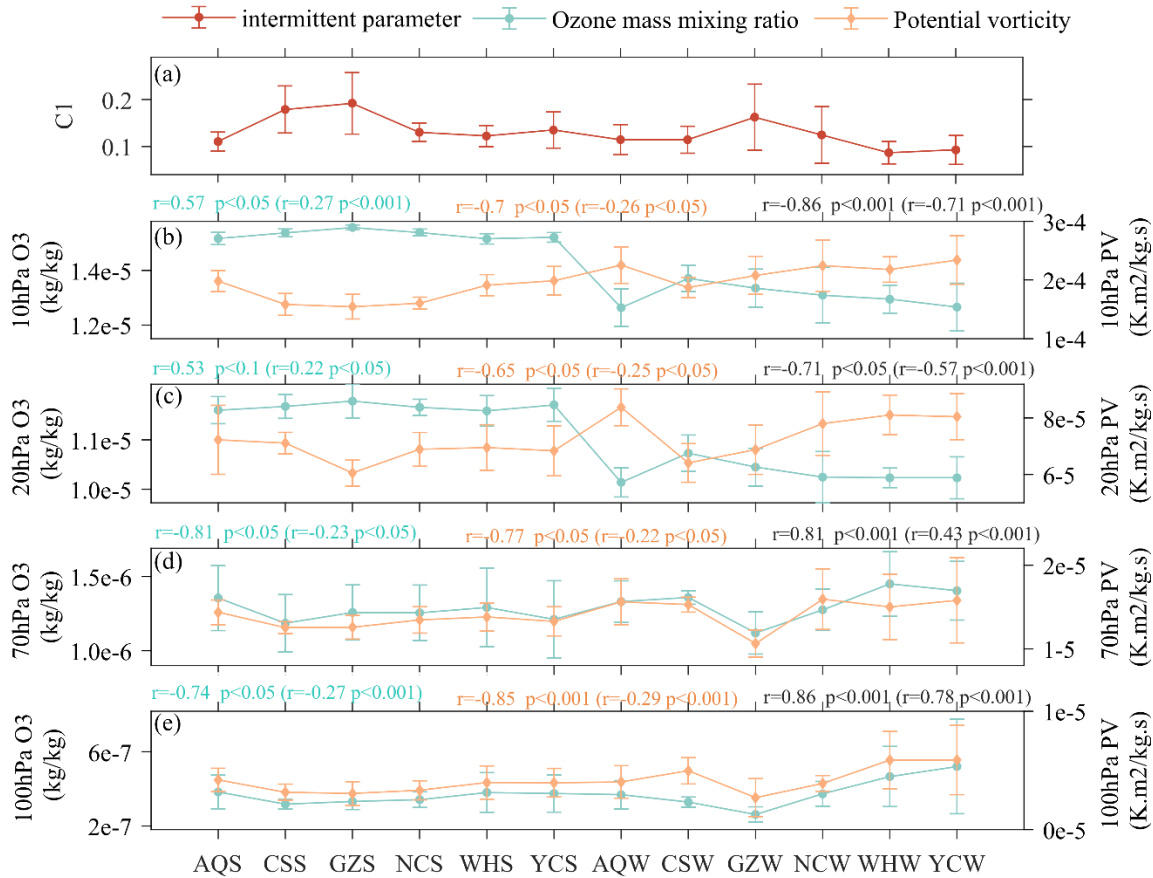
Figure 8. The error bar diagram of (a) intermittent parameters C1, the ozone mass mixing ratio (OMR) and potential vorticity (PV)
300 **at (b) 10hPa, (c) 20hPa, (d) 70hPa, and (e) 100hPa pressure layers in summer (S) and autumn (W), showing a total of 12 clusters over the six sites. The blue, yellow, and black annotations marked at the top of the subgraph indicate the Pearson correlation coefficient and significance level for OMR versus C1, PV versus C1, and OMR versus PV, respectively. Outside the brackets is the correlation of the average values of the 12 clusters (12 values), inside the brackets is the correlation of all cases of the twelve clusters.**

305
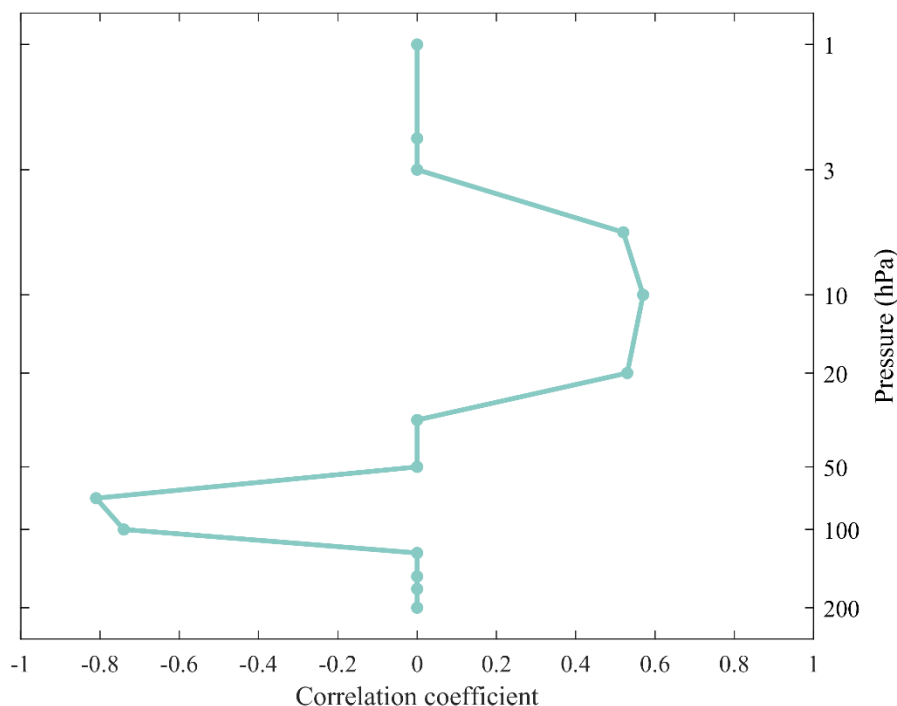
Figure 9. The vertical distribution of correlation coefficient between the OMR and C1 in summer and autumn (a total of twelve clusters) over the six sites at different pressure layers. When the correlation for OMR versus C1 of the average values of the 12 clusters (12 values) and of all cases are both statistically significant (p < 0.1), it is considered that the small-scale GW disturbance is closely related to the change in ozone concentration on the corresponding pressure layers, otherwise the correlation coefficient is set to 0. The significant positive (negative) correlation between C1 and ozone above (below) means that the stronger SGW, the more (less) the ozone concentration above (below).

The three-stage detection process by RITSS and the mechanism diagram of ozone transport and energy transfer are shown in Figure 10. The stratospheric SGWs detected here are closely related to KHI, and previous studies have also confirmed this (He et al., 2020b; Lu and Koch, 2008). The transport capacity of IGW on ozone is weakened due to the critical layer filtering during its upward propagation. In contrast, the high-frequency SGW can propagate to higher altitudes (Dong et al., 2023). Ozone transport that closely related to the SGW occurs between 100hPa and 10hPa, corresponding to the weakening of IGWs in the lower stratosphere (100hPa) and the enhancement of SGWs excited by KHI. SGWs with higher phase velocities would propagate upward without encountering critical level and thus complete the ozone transport to the middle stratosphere (10hPa) (Heale and Snively, 2015; Li et al., 2020; He et al., 2022b). The enhanced intermittency is accompanied by the weakening of IGW energy below, which also reveals the energy transfer from large-scale to small-scale waves.

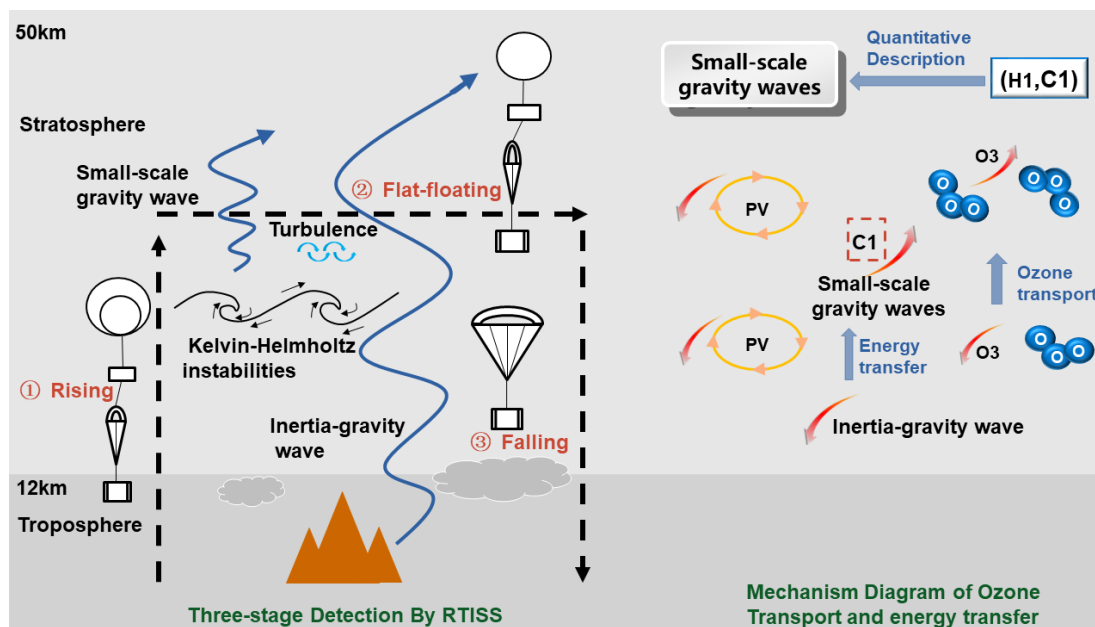**Figure 10. The three-stage detection process by RITSS and the mechanism diagram of ozone transport and energy transfer.**

5 Conclusions

330   Based on the round-trip intelligent sounding system (RTISS) released in China, we conducted a systematic analysis on the atmospheric disturbance information in the stratosphere. Using the structure function and singular measurement, the parameter space (H1, C1) is calculated to describe the nonstationarity and intermittency of atmospheric dynamic processes. The physical process corresponding to the stratospheric SGW is mapped to this parameter space, realizing the comparison of disturbance characteristics between different cases (different in flat-floating height, time and area). There is a significant linear

335   relationship between H1 and height. As the height increases, the nonstationarity (roughness) decreases. In contrast, the distribution of C1 is more random and independent of height, and the intensity of turbulence mixing and SGW at different altitudes can be compared.

        The continuous detection from rising and flat-floating stages realizes the seamless capture of stratospheric SGWs and IGWs below them. By analyzing the correlation between the parameters calculated by multiple-scale disturbances, the

340   connection between IGWs and SGWs is qualitatively revealed. The results show that the enhancement of SGWs is accompanied by the weakening of IGWs activity below, and the generation of these SGWs is closely related to KHI. In addition, we explored the role of GWs in stratospheric ozone transport based on the potential relationship between intermittent parameter C1, potential vorticity and ozone, and found that the enhancement of SGWs is conducive to the transport of ozone from lower stratosphere to higher altitudes, although the length of this path is limited due to wave dissipation. This is the first time that

345   high-frequency, long-duration in situ detection method has been used to discuss the role of stratospheric multi-scale disturbances in energy transfer and material transport in China. The introduction of flat-floating information provides a new idea for the study of stratospheric dynamic processes, while the three-stage detection supplements the research of stratospheric-tropospheric interaction (Scaife et al., 2012; Xie et al., 2012).

       Encouragingly, the quantitative description of SGWs in the stratosphere using (H1, C1) has shown an obvious connection

350   with larger-scale IGWs and smaller-scale turbulence, and a close relationship between it and stratospheric ozone transport can be found. Our results reveal the important role of stratospheric SGWs in material transport and energy transfer, and demonstrate the potential ability of physical parameter space (H1, C1) in stratospheric dynamics research. Follow-up research is worth continuing, using the detection results of RTISS in more regions with longer periods, to improve the understanding about the statistical characteristics and regional differences of stratospheric disturbance information. Besides, the possible "fingerprint"

355   of this parameter space in the material transport of other components (such as water vapor, carbon dioxide, methane, etc) in the stratosphere also deserves further attention.

Appendix A
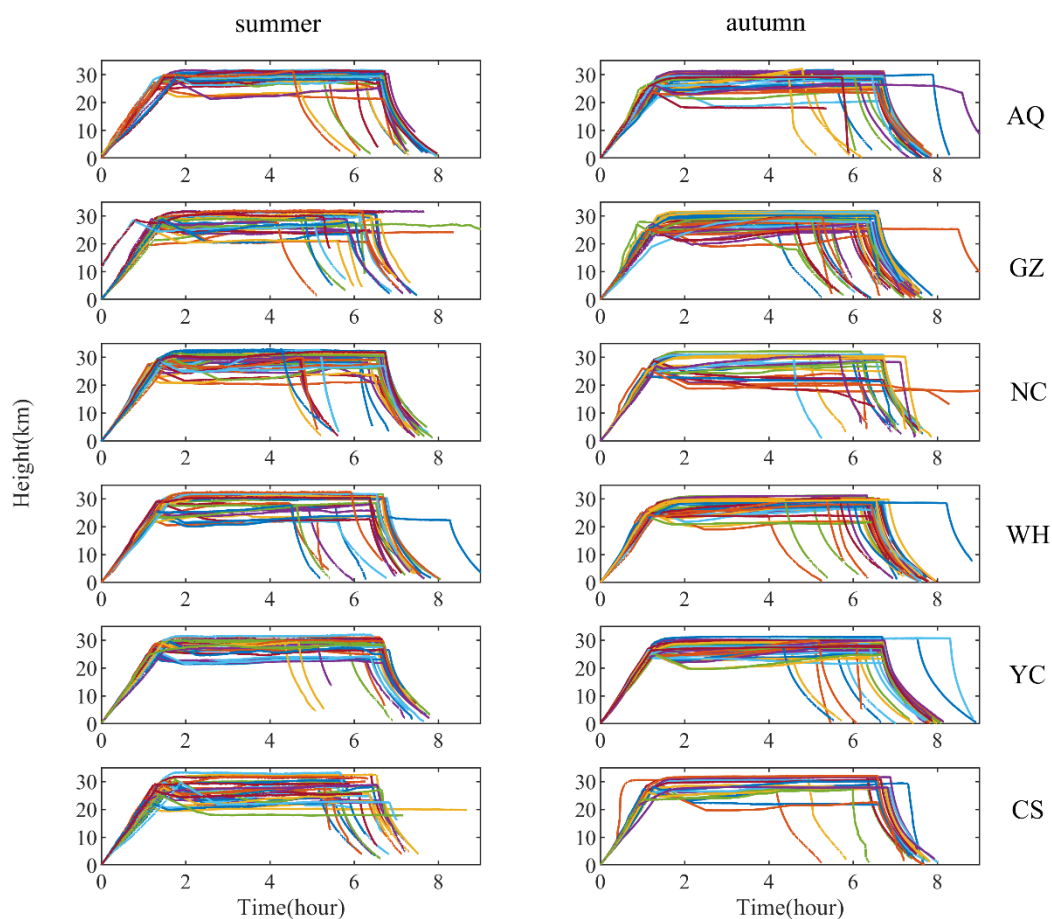
Figure A1. Time-height curves in summer (left) and autumn (right) during the entire detection process for RITSST detections at six sites.

Code and data availability

ERA5 dataset is publicly available through https://doi.org/10.24381/cds.adbb2d47. The procedures and the data files needed to recreate the figures can be download in 4TU.Centre for Research Data. Software and data used in this manuscript are deposited through https://doi.org/10.4121/7c37ae88-0215-4803-8403-57e48088ff0f.

Author contributions

Zheng Sheng, Yang He, Xiaoqian Zhu, and Mingyuan He initiated the study. Zheng Sheng designed the scheme, Yang He analyzed data and drew figures, Yang He and Zheng Sheng wrote the manuscript. All the authors interpreted results and revised the manuscript.

19

Competing interests

The contact author has declared that neither of the authors has any competing interests.

Acknowledgments

References

Abdilghanie, A. M. and Diamessis, P. J.: The internal gravity wave field emitted by a stably stratified turbulent wake, J. Fluid Mech., 720, 104–139, 2013.

Alexander, M. J., Geller, M., McLandress, C., Polavarapu, S., Preusse, P., Sassi, F., Sato, K., Eckermann, S., Ern, M., Hertzog, A., Kawatani, Y., Pulido, M., Shaw, T. A., Sigmond, M., Vincent, R., and Watanabe, S.: Recent developments in gravity-wave effects in climatemodels and the global distribution of gravity-wavemomentum flux from observations and models, Q. J. R. Meteorol. Soc., 136, 1103–1124, https://doi.org/10.1002/qj.637, 2010.

Alexander, M. J., Liu, C. C., Bacmeister, J., Bramberger, M., Hertzog, A., and Richter, J. H.: Observational Validation of Parameterized Gravity Waves From Tropical Convection in the Whole Atmosphere Community Climate Model, J. Geophys. Res. Atmos., 126, https://doi.org/10.1029/2020JD033954, 2021.

Alexander, S. P., Orr, A., Webster, S., and Murphy, D. J.: Observations and fine-scale model simulations of gravity waves over Davis, East Antarctica (69S, 78E), J. Geophys. Res. Atmos., 122, 7355–7370, 2017.

Allen, S. J. and Vincent, R. A.: Gravity wave activity in the lower atmosphere: seasonal and latitudinal variations, J. Geophys. Res., 100, 1327–1350, https://doi.org/10.1029/94JD02688, 1995.

Andreas, K., Rolf, P., Gonzague, R., Hurst, D. F., Hall, E. G., and Jordan, A. F.: Controlled weather balloon ascents and descents for atmospheric research and climate monitoring, Atmos. Meas. Tech., 9, 929–938, 2016.

Cao, X., Guo, Q., and Yang, R.: Research of rising and falling twice sounding based on long-time interval of flat-floating, Yi Qi Yi Biao Xue Bao/Chinese J. Sci. Instrum., https://doi.org/10.19650/j.cnki.cjsi.J1803748, 2019.

Cho, J. Y. N. and Lindborg, E.: Horizontal velocity structure functions in the upper troposphere and lower stratosphere 1. Observations, J. Geophys. Res. Atmos., 106, 10223–10232, https://doi.org/10.1029/2000JD900814, 2001.

Dong, W., Fritts, D. C., Liu, A. Z., Lund, T. S., and Liu, H.: Gravity Waves Emitted From Kelvin-Helmholtz Instabilities, Geophys. Res. Lett., 50, e2022GL102674, https://doi.org/10.1029/2022GL102674, 2023.

400 Eckermann, S. D.: Effect of background winds on vertical wavenumber spectra of atmospheric gravity waves, J. Geophys. Res., 100, https://doi.org/10.1029/95jd00987, 1995.

Eckermann, S. D., Hirota, I., and Hocking, W. K.: Gravity wave and equatorial wave morphology of the stratosphere derived from long-term rocket soundings, Q. J. R. Meteorol. Soc., 121, 149–186, https://doi.org/10.1002/qj.49712152108, 1995.

Fritts, D. C. and Alexander, M. J.: Gravity wave dynamics and effects in the middle atmosphere, Rev. Geophys., 41, 1003, 405 https://doi.org/10.1029/2001RG000106, 2003.

Fritts, D. C. and Alexander, M. J.: Correction to "Gravity wave dynamics and effects in the middle atmosphere," Rev. Geophys., 50, https://doi.org/10.1029/2012rg000409, 2012.

Guo, J., Liu, B., Gong, W., Shi, L., Zhang, Y., Ma, Y., Zhang, J., Chen, T., Bai, K., and Stoffelen, A.: Technical note: First comparison of wind observations from ESA's satellite mission Aeolus and ground-based radar wind profiler network of 410 China, Atmos. Chem. Phys., 21, 2945–2958, 2021.

He, Y., Sheng, Z., and He, M.: The First Observation of Turbulence in Northwestern China by a Near-Space High-Resolution Balloon Sensor, Sensors, 677, 1–17, https://doi.org/10.3390/s20030677, 2020a.

He, Y., Sheng, Z., and He, M.: The Interaction Between the Turbulence and Gravity Wave Observed in the Middle Stratosphere Based on the Round-Trip Intelligent Sounding System, Geophys. Res. Lett., 47, 1–10, 415 https://doi.org/10.1029/2020GL088837, 2020b.

He, Y., Zhu, X. Q., Sheng, Z., Ge, W., Zhao, X. R., and He, M. Y.: Atmospheric Disturbance Characteristics in the Lower-middle Stratosphere Inferred from Observations by the Round-Trip Intelligent Sounding System (RTISS) in China, Adv. Atmos. Sci, 39, 131–144, https://doi.org/10.1007/s00376-021-1110-2.View, 2022a.

He, Y., Zhu, X., Sheng, Z., He, M., and Feng, Y.: Observations of Inertia Gravity Waves in the Western Pacific and Their 420 Characteristic in the 2015/2016 Quasi-Biennial Oscillation Disruption, J. Geophys. Res. Atmos., 127, 2022b.

Heale, C. J. and Snively, J. B.: Gravity wave propagation through a vertically and horizontally inhomogeneous background wind, J. Geophys. Res. Atmos., 120, 5931–5950, 2015.

Hertzog, A., Boccara, G., Vincent, R. A., and Vial, F.: Estimation of gravity wave momentum flux and phase speeds from quasi-lagrangian stratospheric balloon flights. Part I: Theory and simulations, J. Atmos. Sci., 65, 3042–3055, 425 https://doi.org/10.1175/2008JAS2709.1, 2008.

Hertzog, A., Alexander, J. M., and Plougonven, R.: On the intermittency of gravity wave momentum flux in the stratosphere, J. Atmos. Sci., 69, 3433–3448, https://doi.org/10.1175/JAS-D-12-09.1, 2012.

Huang, K. M., Liu, A. Z., and Zhang, S. D.: Simultaneous upward and downward propagating inertia-gravity waves in the MLT observed at Andes Lidar Observatory, J. Geophys. Res. Atmos., 122, 2812–2830, 2017.

430   Jorge, T., Brunamonti, S., Poltera, Y., Wienhold, F. G., Luo, B. P., Oelsner, P., Hanumanthu, S., Singh, B. B., Krner, S., and

Dirksen, R.: Understanding balloon-borne frost point hygrometer measurements after contamination by mixed-phase clouds,

Atmos. Meas. Tech., 2021.

Kalashnik, M. V. and Chkhetiani, O. G.: Generation of gravity waves by singular potential vorticity disturbances in shear

flows, J. Atmos. Sci., 74, 293–308, https://doi.org/10.1175/JAS-D-16-0134.1, 2017.

435   Kim, Y. J., Eckermann, S. D., and Chun, H. Y.: An overview of the past, present and future of gravity-wave drag

parametrization for numerical climate and weather prediction models, Atmos. - Ocean, 41, 65–98,

https://doi.org/10.3137/ao.410105, 2003.

Kinoshita, T., Shirooka, R., Suzuki, J., Ogino, S., Iwasaki, S., Yoneyama, K., Haryoko, U., Ardiansyah, D., and Alyudin, D.:

A study of gravity wave activities based on intensive radiosonde observations at Bengkulu during YMC-Sumatra 2017, IOP

440   Conf. Ser. Earth Environ. Sci., 303, https://doi.org/10.1088/1755-1315/303/1/012011, 2019.

Ko, H. C. and Chun, H. Y.: Potential sources of atmospheric turbulence estimated using the Thorpe method and operational

radiosonde data in the United States, Atmos. Res., 265, 105891, https://doi.org/10.1016/j.atmosres.2021.105891, 2022.

Laroche, S., Sarrazin, and R.: Impact of radiosonde balloon drift on numerical weather prediction and verification, Weather

Forecast., 2013.

445   Li, J., Li, T., Wu, Q., Tang, Y., Wu, Z., and Cui, J.: Characteristics of Small-Scale Gravity Waves in the Arctic Winter

Mesosphere, J. Geophys. Res. Sp. Phys., 125, e2019JA027643, 2020.

Lindborg, E.: Can the atmospheric kinetic energy spectrum be explained by two-dimensional turbulence?, J. Fluid Mech.,

388, 259–288, https://doi.org/10.1017/S0022112099004851, 1999.

Lu, C. and Koch, S. E.: Interaction of upper-tropospheric turbulence and gravity waves as obtained from spectral and

450   structure function analyses, J. Atmos. Sci., 65, 2676–2690, https://doi.org/10.1175/2007JAS2660.1, 2008.

Lv, Y., Guo, J., Cao, L., Li, J., and Huang, G.: Spatiotemporal characteristics of atmospheric turbulence over China

estimated using operational high-resolution soundings, Environ. Res. Lett., 16, 054050, 2021.

Marshak, A., Davis, A., Wiscombe, W., and Cahalan, R.: Scale invariance in liquid water distributions in marine

stratocumulus. Part II: Multifractal properties and intermittency issues, J. Atmos. Sci., 54, 1423–1444,

455   https://doi.org/10.1175/1520-0469(1997)054<1423:SIILWD>2.0.CO;2, 1997.

Moffat-Griffin, T., Jarvis, M. J., Colwell, S. R., Kavanagh, A. J., Manney, G. L., and Daffer, W. H.: Seasonal variations in

lower stratospheric gravity wave energy above the Falkland Islands, J. Geophys. Res. Atmos., 118, 10861–10869,

https://doi.org/10.1002/jgrd.50859, 2013.

Plougonven, R., de la Cámara, A., Hertzog, A., and Lott, F.: How does knowledge of atmospheric gravity waves guide their

460   parameterizations?, Q. J. R. Meteorol. Soc., 146, 1529–1543, https://doi.org/10.1002/qj.3732, 2020.

Scaife, A. A., Thomas, S., David R.Fereday, and Ulrich, C.: Climate change projections and stratosphere–troposphere

interaction, Clim. Dyn., 38, 2089–2097, 2012.

SPARC: SPARC, 2022: SPARC Reanalysis Intercomparison Project (S-RIP) Final Reportt. Masatomo Fujiwara, Gloria L. Manney, Lesley J. Gray, and Jonathon S. Wright (Eds.), SPARC Rep. No. 10, WCRP-6/2021, 2022.

465   Stephen A, C., Hock, T., and Cocquerez, P.: Driftsondes: Providing In Situ Long-Duration Dropsonde Observations over Remote Regions, Bull. Am. Meteorol. Soc., 94, 1661–1674, 2015.

Tian, W., Huang, J., ZHANG, J., XIE, F., WANG, W., PENG, Y., and Citation: Role of Stratospheric Processes in Climate Change: Advances and Challenges, Adv. Atmos. Sci., https://doi.org/10.1007/s13351-020-9839-6.View, 2023.

Wilson, R., Dalaudier, F., and Luce, H.: Can one detect small-scale turbulence from standard meteorological radiosondes?,

470   Atmos. Meas. Tech., 4, 795–804, https://doi.org/10.5194/amt-4-795-2011, 2011.

Wright, C. J., Hindley, N. P., and Mitchell, N. J.: Combining AIRS and MLS observations for three-dimensional gravity wave measurement, Geophys. Res. Lett., 43, 884–893, https://doi.org/10.1002/2015GL067233, 2016.

Xie, F., Li, J., Tian, W., Feng, J., and Huo, Y.: Signals of El Niño Modoki in the tropical tropopause layer and stratosphere, Atmos. Chem. Phys., 12, 5259–5273, 2012.

475   Zhang, F., Wei, J., Zhang, M., Bowman, K. P., Pan, L. L., Atlas, E., and Wofsy, S. C.: Aircraft measurements of gravity waves in the upper troposphere and lower stratosphere during the START08 field experiment, Atmos. Chem. Phys., 15, 7667–7684, https://doi.org/10.5194/acp-15-7667-2015, 2015.

Zhang, J., Zhang, S. D., Huang, C. M., Huang, K. M., Gong, Y., Gan, Q., and Zhang, Y. H.: Statistical Study of Atmospheric Turbulence by Thorpe Analysis, https://doi.org/10.1029/2018JD029686, 2019.

480